Fast elementary gates for universal quantum computation with Kerr parametric oscillator qubits

Taro Kanao [*] and Hayato Goto

Frontier Research Laboratory, Corporate Research & Development Center,
Toshiba Corporation, 1 Komukai-Toshiba-cho, Saiwai-ku, Kawasaki 212-8582, Japan

Kerr parametric oscillators (KPOs) can stabilize the superpositions of coherent states, which can be utilized as qubits, and are promising candidates for realizing hardware-efficient quantum computers. Although elementary gates for universal quantum computation with KPO qubits have been proposed, these gates are usually based on adiabatic operations and thus need long gate times, which result in errors caused by photon loss in KPOs realized by, e.g., superconducting circuits. In this work we accelerate the elementary gates by experimentally feasible control methods, which are based on numerical optimization of pulse shapes for shortcuts to adiabaticity. By numerical simulations, we show that the proposed methods can achieve speedups compared to adiabatic ones by up to six times with high gate fidelities of 99.9%. These methods are thus expected to be useful for quantum computers with KPOs.

I. INTRODUCTION

Towards hardware-efficient quantum computing, qubits with stabilized coherent states have been proposed [1,2]. Coherent states with opposite phases and their superposition, the so-called Schrödinger cat state [3,4], can be stabilized in a parametric oscillator with engineered two-photon dissipation [2,5] or Kerr nonlinearity [1,6–10], which are referred to as a dissipative-cat qubit or a Kerr-cat qubit, respectively. The latter is also called a Kerr parametric oscillator (KPO) qubit [7,11–16]. In these qubits, when the two coherent states are used as the computational basis, bit-flip errors can be suppressed, because a coherent state is robust against photon loss [1,2,9]. The stabilization of the coherent states and the suppression of bit-flip errors have been experimentally realized in superconducting circuits for the dissipative-cat qubit [17,18] and the KPO qubit [12,19].

A KPO does not rely on dissipation and can be described by a simple Hamiltonian. Despite the simplicity, KPOs yield rich nonlinear dynamics such as quantum bifurcation [1,7,9] and chaos [20–22]. The quantum bifurcation can be applied to quantum annealing [7] and a number of its implementations have been proposed [11,23–29]. By regarding two branches of the bifurcation as up- and down-spin states, a KPO lattice can behave like an Ising model, and its physics, such as phase transitions, has been studied [30–36]. Other theoretical results on KPOs have been reported, such as exact solutions [37,38], state generations [39–43], measurements and outputs [44–47],

excited-state quantum phase transitions [48,49], controls under a strong pump field [50], engineered dissipation [51–53], a four-photon KPO [16], symmetries [54], and Floquet theory [55].

Applications of KPOs to fault-tolerant quantum computing [56] have also been studied [57]. Quantum gates preserving the bias of errors mentioned above have been proposed [58], which can be utilized for hardware-efficient quantum error correction [59]. Analytically engineered control methods for shortening the gate times of the bias-preserving gates have recently been proposed [13]. Furthermore, for noisy intermediate-scale quantum (NISQ) applications [60], variational quantum algorithms [61,62] for KPOs have been proposed, such as quantum supervised machine learning [63] and a quantum approximate optimization algorithm [64].

For implementing a KPO with a superconducting circuit, a Josephson parametric oscillator [65–67] with low photon loss has been suggested [7,9] and demonstrated experimentally [12]. Then, by using a KPO in a three-dimensional cavity, single-qubit gates have been performed [19]. Also, tunable coupling between two KPOs has been realized [68]. Other experiments with KPOs have been reported, such as a crossover from a Duffing oscillator to a KPO [14], degenerate excited states [69,70], single-qubit operations and characterizations with an ancillary transmon [71], and reflection coefficient measurements [72].

For KPO qubits, elementary gates for universal quantum computation have been proposed [8,9], which are based on adiabatic evolution and consist of Z, X, and ZZ rotations denoted by R_z, R_x, and R_{zz}, respectively. Experimentally, a study [19] has demonstrated adiabatic R_z and nonadiabatic R_x, and another study [71] has adiabatically performed both R_z and R_x. Theoretically, other kinds of gate implementations have been proposed [15,73–77].

Shorter gate times are desirable, because they can reduce errors caused by photon loss in KPOs and also enable

---

*taro.kanao@toshiba.co.jp

faster computation. However, the previous adiabatic elementary gates [8,9] need long gate times and otherwise diabatic transitions out of a qubit space cause leakage errors. To reduce leakage errors, in this work we focus on control methods called shortcuts to adiabaticity (STAs) [78]. For KPOs, STAs have been proposed for cat-state generation [9,40] and R_{zz} with a phase rotation of a parametric drive [15]. Also, a variant of the derivative removal by adiabatic gate (DRAG) technique, which is related to STAs, has been proposed for the bias-preserving gates [13].

To accelerate the elementary gates for universal quantum computation with KPO qubits, our approach is based on an STA called counterdiabatic terms (or counterterms for short) [79,80], but does not use the exact counterterms, which are often experimentally infeasible. Instead, we first approximate the counterterms by experimentally feasible terms [81] and then numerically optimize the pulse shapes for the gate operations. As a result, we successfully shorten gate times, keeping high gate fidelities. By this approach, the gate operations become faster by 2.6 times for R_z, 6.0 times for R_{zz}, and 2.6 times or higher for R_x than the previous adiabatic ones [8]. Interestingly, the states of KPOs during the optimized gate operations for the shortest gate times are not necessarily instantaneous eigenstates, which indicates that the numerical optimization explores gate operations beyond the STA. We also numerically show that the optimized gate operations are robust against systematic errors in the amplitudes of gate pulses and the shortened gate times can suppress errors caused by single-photon loss. We expect that these optimized elementary gates for KPO qubits will be useful for NISQ applications in the near term and fault-tolerant quantum computation in the long term.

II. APPROXIMATE STA

A. Elementary gates for KPO qubits

We first introduce the model of the KPO and elementary gates for universal quantum computation with the KPO qubits [7,9]. In a rotating frame and within the rotating-wave approximation, the Hamiltonian for a KPO is given by [6]

$$H_{KPO} = -\frac{K}{2}a^{\dagger 2}a^2 + \frac{p}{2}(a^{\dagger 2} + a^2), \tag{1}$$

where a, K, and p are the annihilation operator, the Kerr coefficient, and the amplitude of a parametric drive, respectively. In this study the reduced Planck constant $\hbar$ is set to 1. The two degenerate eigenstates of the Hamiltonian corresponding to effective ground states of the KPO [73] are written as

$$|C_\pm\rangle = \frac{1}{\sqrt{2(1 \pm e^{-2\alpha^2})}}(|\alpha\rangle \pm |-\alpha\rangle), \tag{2}$$

where $|\pm\alpha\rangle$ are coherent states with an amplitude $\alpha = \sqrt{p/K}$. In this work we use the computational basis states [58,73]

$$|\tilde{0}\rangle = \frac{1}{\sqrt{2}}(|C_+\rangle + |C_-\rangle), \tag{3}$$

$$|\tilde{1}\rangle = \frac{1}{\sqrt{2}}(|C_+\rangle - |C_-\rangle), \tag{4}$$

which are exactly orthogonal. Equations (3) and (4) are approximately equal to $|\pm\alpha\rangle$, respectively, for $p/K = 4$ used in this study.

For the KPO qubits, elementary gates for universal computation can consist of Z, X, and ZZ rotations, which are expressed as [56]

$$R_z(\phi) = \begin{pmatrix} e^{-i\phi/2} & 0 \\ 0 & e^{i\phi/2} \end{pmatrix}, \tag{5}$$

$$R_x(\theta) = \begin{pmatrix} \cos\frac{\theta}{2} & -i\sin\frac{\theta}{2} \\ -i\sin\frac{\theta}{2} & \cos\frac{\theta}{2} \end{pmatrix}, \tag{6}$$

$$R_{zz}(\Theta) = \begin{pmatrix} e^{-i\Theta/2} & 0 & 0 & 0 \\ 0 & e^{i\Theta/2} & 0 & 0 \\ 0 & 0 & e^{i\Theta/2} & 0 \\ 0 & 0 & 0 & e^{-i\Theta/2} \end{pmatrix}, \tag{7}$$

respectively, where ϕ, θ, and Θ are the respective rotation angles. For universal computation, arbitrary ϕ, $\theta = \pi/2$, and $\Theta = \pi/2$ are enough [8,9,56]. For KPOs, these elementary gates can be implemented based on adiabatic control with a single-photon drive, a detuning, and a linear coupling, respectively. The Hamiltonians corresponding to the single-qubit gates are

$$H_0(t) = H_{KPO} + g_0(t)A_0, \tag{8}$$

$$A_0 = a^\dagger + a \quad \text{for } R_z, \tag{9}$$

$$A_0 = a^\dagger a \quad \text{for } R_x, \tag{10}$$

where $g_0(t)$ is the amplitude of a gate pulse. A linear coupling necessary for R_{zz} can be realized with beam-splitter coupling [8,9] or two-mode squeezing [13], described by

$$H_0(t) = H_{KPO1} + H_{KPO2} + g_0(t)A_0, \tag{11}$$

$$A_0 = a_1^\dagger a_2 + a_2^\dagger a_1 \quad \text{for beam-splitter coupling}, \tag{12}$$

$$A_0 = a_1^\dagger a_2^\dagger + a_1 a_2 \quad \text{for two-mode squeezing}, \tag{13}$$

where a_i and H_{KPOi} are the annihilation operator and the Hamiltonian in Eq. (1) for the ith KPO.

B. Approximate counterterms for STAs

An ideal counterterm $H_1(t)$ for STAs exactly reproduces adiabatic evolution with $H_0(t)$ by finite-time evolution with $H_0(t) + H_1(t)$ [78–80], but is often experimentally infeasible. In this work we approximate $H_1(t)$ by the terms that can be realized in experiments as

$$H_1(t) \simeq \frac{i\dot{g}_0(t)}{4K\alpha^2}(a^\dagger - a) \quad \text{for } R_z, \tag{14}$$

$$H_1(t) \simeq \frac{i\dot{g}_0(t)}{4K\alpha^2}(a^{\dagger 2} - a^2) \quad \text{for } R_x, \tag{15}$$

$$H_1(t) \simeq \frac{i\dot{g}_0(t)}{2K\alpha^2}(a_1^\dagger a_2^\dagger - a_1 a_2) \quad \text{for } R_{zz}, \tag{16}$$

where the overdots denote the time derivative (see Appendix A for the details of the assumptions and derivations). These $H_1(t)$ correspond to the following experimental operations.

(i) The $H_1(t)$ for R_z in Eq. (14) can be implemented with a single-photon drive with its phase shifted by $\pi/2$ from the original single-photon drive in Eq. (9).

(ii) The $H_1(t)$ for R_x in Eq. (15) can be realized by a two-photon drive with its phase shifted by $\pi/2$ from the original parametric drive.

(iii) The $H_1(t)$ for R_{zz} in Eq. (16) is another two-mode squeezing in addition to the original one in Eq. (13), which can be realized in a previously proposed superconducting circuit for R_{zz} [74].

Note that the counterterm in Eq. (16) can be derived from both R_{zz} by the beam-splitter coupling in Eq. (12) and R_{zz} by the two-mode squeezing in Eq. (13). However, we numerically find that the two-mode squeezing in Eq. (13) gives better results with the counterterm in Eq. (16), because this counterterm is a two-mode squeezing and can better cancel unwanted transitions caused by the two-mode squeezing in Eq. (13) than the beam-splitter coupling in Eq. (12) [see Appendix B 1 for an explanation using the matrix elements of A_0 and $H_1(t)$]. We thus use the two-mode squeezing in Eq. (13) in the following.

Here we also comment on another candidate of a counterterm for R_{zz},

$$H_1(t) \propto i(a_1^\dagger a_2 - a_2^\dagger a_1). \tag{17}$$

We numerically found that this term does not work as a counterterm (a similar result was mentioned in Ref. [13]). Equation (17) does not cancel unwanted transitions out of the qubit space, because $H_1(t)$ in Eq. (17) and A_0 in Eqs. (12) and (13) have different permutation symmetry, namely, symmetry with respect to the interchange of KPO1 and KPO2 (see Appendix B 1 for details).

C. Numerical optimization

To go beyond the analytic approximate $H_1(t)$ in Eqs. (14)–(16), our proposed approach uses arbitrary waveforms for the amplitudes of the counterpulses $g_1(t)$ as

$$H_1(t) = g_1(t)A_1, \tag{18}$$

$$A_1 = i(a^\dagger - a) \quad \text{for } R_z, \tag{19}$$

$$A_1 = i(a^{\dagger 2} - a^2) \quad \text{for } R_x, \tag{20}$$

$$A_1 = i(a_1^\dagger a_2^\dagger - a_1 a_2) \quad \text{for } R_{zz}, \tag{21}$$

and numerically optimizes $g_1(t)$ as well as $g_0(t)$ in Eqs. (8) and (11). Total Hamiltonians are then given by, for the single- and two-qubit gates, respectively,

$$H(t) = H_{\mathrm{KPO}} + g_0(t)A_0 + g_1(t)A_1, \tag{22}$$

$$H(t) = H_{\mathrm{KPO1}} + H_{\mathrm{KPO2}} + g_0(t)A_0 + g_1(t)A_1, \tag{23}$$

where A_0 are given in Eqs. (9), (10), and (13). Here the two-mode squeezing Hamiltonian in Eq. (13) is used as mentioned above. We expect that this approach, which numerically optimizes pulse shapes for STAs, will be useful for other qubit systems.

To optimize $g_0(t)$ and $g_1(t)$ numerically, we express the waveforms of the pulse amplitudes as [82]

$$g_0(t) = \sum_{n=1}^{N_f} \left[g_{0,2n-1} \sin \frac{(2n-1)\pi t}{T} \right.$$
$$\left. + \frac{g_{0,2n}}{2} \left(1 - \cos \frac{2\pi n t}{T} \right) \right], \tag{24}$$

$$g_1(t) = \sum_{n=1}^{N_f} g_{1,n} \sin \frac{2\pi n t}{T}, \tag{25}$$

where T is a gate time and N_f determines the number of frequency components. Equations (24) and (25) give experimentally realistic waveforms, because the highest frequencies in $g_j(t)$ are limited to N_f/T, and $g_j(t)$ are zero at initial and final times ($t = 0, T$). We choose the symmetric $g_0(t)$ and antisymmetric $g_1(t)$ with respect to time reversal $t \to T - t$, because an exact counterterm is antisymmetric when the other term is symmetric (see Appendix B 2). In $g_0(t)$ we include the sine terms to allow for nonzero $\dot{g}_0(t)$ at $t = 0, T$ [8].

We numerically optimize $g_{j,n}$ in Eqs. (24) and (25) to maximize an average gate fidelity $\bar{F}$ [83,84] given in Eq. (C1) in Appendix C, using the quasi-Newton method with the Broyden-Fletcher-Goldfarb-Shanno formula (a nonlinear programming solver FMINUNC in MATLAB). We set the initial values of $g_{j,n}$ for the optimization to the ones corresponding to analytic waveforms for adiabatic elementary gates without and with the counterterms in Eqs. (14)–(16) (see Appendix D).

Here we summarize the proposed method in Sec. II. The method uses the Hamiltonians in Eqs. (22) and (23) with the operators A_0 in Eqs. (9), (10), and (13) and A_1 in Eqs. (19)–(21) and numerically optimizes the waveforms for $g_0(t)$ and $g_1(t)$. The proposed method is expected to be experimentally feasible, because the operations corresponding to A_0 and A_1 can be implemented with the microwave drives mentioned above and their amplitudes $g_0(t)$ and $g_1(t)$ have the realistic waveforms in Eqs. (24) and (25), respectively.

III. NUMERICAL SIMULATIONS

In the present simulation, we regard the Kerr coefficient K as the unit of frequency and set the amplitude of the parametric drive to $p = 4K$, which corresponds to the mean photon number of 4. This p is chosen for the following reasons. First, a smaller p causes non-negligible overlap between the two coherent states $\langle \alpha | -\alpha \rangle$, which cannot be used as a well-defined qubit. Second, a larger p would increase unwanted effects such as the violation of the rotating-wave approximation [50] and errors caused by photon loss in realistic KPOs. We thus choose a typical intermediate value, $p = 4K$ [8].

We express states and operators in the photon-number basis with the largest photon number of 40, which is large enough. We simulate the time evolution of states by numerically solving the Schrödinger equation

$$i|\dot{\psi}\rangle = H(t)|\psi\rangle, \tag{26}$$

unless stated otherwise. We use the fourth-order Runge-Kutta method with the step size of $10^{-4}/K$.

We compare the following four cases depending on the waveforms and the counterterms: (i) analytic waveforms

without the counterterms, (ii) analytic waveforms with the counterterms in Eqs. (14)–(16), (iii) numerically optimized waveforms in Eq. (24) without the counterterms, and (iv) numerically optimized waveforms in Eqs. (24) and (25) with the counterterms in Eq. (18). For the analytic waveforms, we choose the same ones as the previous study [8]. The analytic waveforms and initial values of $g_{j,n}$ for the numerical optimization are given in Appendix D. The N_f in Eqs. (24) and (25) is set to 10.

A. Simulation results for R_z

Figure 1(a) shows the average infidelities $1 - \bar{F}$ for $R_z(\pi)$ plotted as a function of the dimensionless gate time KT. The infidelities decrease with increasing gate time, indicating the adiabaticity of the gate, where the errors are mainly due to the leakage of population to the states outside the qubit space. We define a minimum gate time $T_{\min}$ by minimal T satisfying $1 - \bar{F} < 10^{-3}$ and compare $T_{\min}$ for the above four cases. With analytic waveforms, the $KT_{\min}$ are 1.3 and 1.2 without and with the counterterm, respectively. By the numerical optimization, the $KT_{\min}$ are shortened to 0.9 and 0.5, respectively. Thus the numerically optimized R_z with the counterterm is 2.6 times faster than the original analytic R_z without the counterterm. These results show that the counterterm is effective and the improvement is enhanced by the numerical optimization.

We examine the optimized gate operation with the counterterm at $KT_{\min} = 0.5$. The optimized waveforms of $g_j(t)$ are shown in Fig. 1(b). Figure 1(c) shows the resulting time evolutions of the mean photon number and population in the qubit space with the initial state $|C_+\rangle$, where P is a projector onto the computational basis states

$$P = |\tilde{0}\rangle\langle\tilde{0}| + |\tilde{1}\rangle\langle\tilde{1}|. \quad (27)$$

It is notable that despite the large amplitudes of $g_j(t)$, the mean photon number and the population in the qubit space are almost unchanged.

To see the state in more detail, we use the Wigner function $W(x, y)$, which is a quasiprobability distribution for ($x = (a + a^\dagger)/2, y = (a - a^\dagger)/2i$) [85] and is calculated by the technique in Ref. [7]. Figure 2 shows $W(x, y)$ during the gate operation with the optimized $g_j(t)$ in Fig. 1(b). The gate operation retains the two peaks around ($x = \pm 2, y = 0$) and the interference fringe between them, which indicate that the state is in the superposition of the coherent states. Only the interference fringe changes with the time, corresponding to the relative phase rotations of $|\tilde{0}\rangle$ and $|\tilde{1}\rangle$. These dynamics are possible because the single-photon drives used for R_z can preserve the coherent states when the effective potential of the KPO is well approximated by the double well [12,57]. Interestingly, we numerically found that the cat states in Fig. 2 are not instantaneous eigenstates of $H_0(t)$, which indicates that our proposed approach is beyond STAs.

We next show that the optimized $g_j(t)$ with the counterterm for $R_z(\pi)$ can be used for $R_z(\phi)$ with arbitrary ϕ by introducing only one time-independent scaling parameter λ. The pulse amplitudes are set to $\lambda g_0(t)$ and $\lambda g_1(t)$. The resulting ϕ is determined by maximizing $\bar{F}$. Figure 3(a) shows $1 - \bar{F}$ as a function of ϕ at $KT_{\min} = 0.5$, which demonstrates that this method gives high-fidelity $R_z(\phi)$ for arbitrary ϕ in
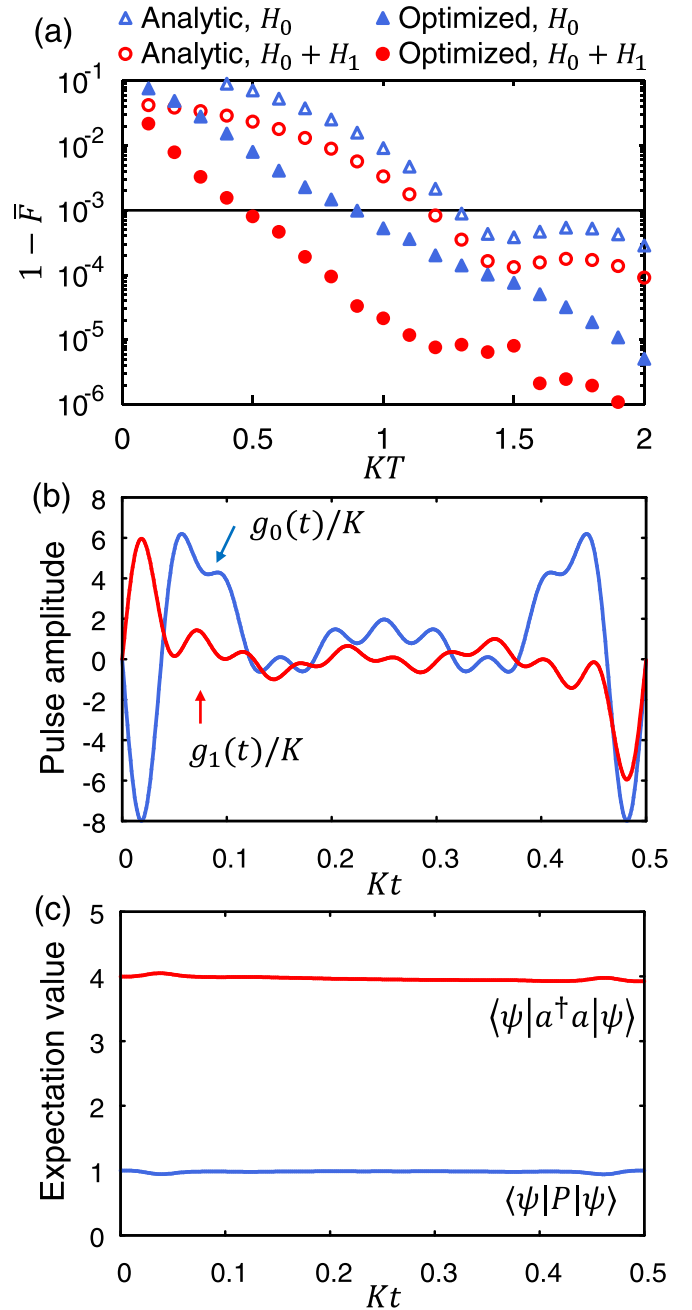

FIG. 1. (a) Plot of average infidelities for $R_z(\pi)$ as a function of gate time for an analytic waveform of a pulse amplitude without a counterterm (Analytic, H_1) and with it (Analytic, $H_1 + H_2$) and for numerically optimized waveforms without the counterterm (Optimized, H_1) and with it (Optimized, $H_1 + H_2$). The line indicates $1 - \bar{F} = 10^{-3}$. (b) Waveforms of the amplitudes of a gate pulse $g_0(t)$ and a counterpulse $g_1(t)$ for $R_z(\pi)$, which are numerically optimized for $KT_{\min} = 0.5$. (c) Mean photon number and population in the qubit space during $R_z(\pi)$ with $g_j(t)$ in (b). The initial state is $|C_+\rangle$.

$0 \leqslant \phi \leqslant \pi$. An exact counterterm suggests that this continuous gate by the one parameter λ is possible because the changes in the states are small during the gate operation as shown in Fig. 2 (see Appendix B 3 for details). On the other hand, this continuous gate does not hold for $R_x(\theta)$, as also
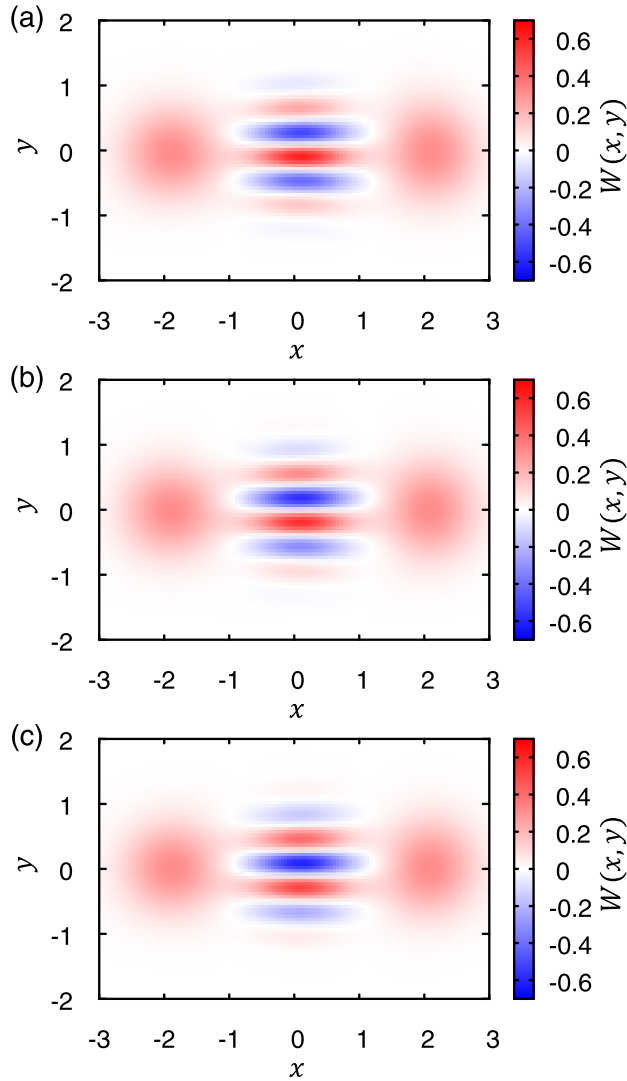
FIG. 2. Wigner functions during $R_z(\pi)$ with the optimized $g_j(t)$ in Fig. 1(b). (a) $Kt = 0.1$, (b) $Kt = 0.25$, and (c) $Kt = 0.4$. The initial state is $|C_+\rangle$.

mentioned later in Sec. III C, where the states largely change during the gate operation.

To examine the optimality and robustness of the optimized $g_j(t)$, we evaluate $R_z(\pi)$ with $(1 + \delta_j)g_j(t)$ for given relative errors δ_j, which can model systematic errors in the pulse amplitudes [15]. Figure 3(b) shows $1 - \bar{F}$ as a function of δ_j. First, at $\delta_0 = \delta_1 = 0$, the gradient of $1 - \bar{F}$ with respect to δ_j vanishes, implying that $\delta_0 = \delta_1 = 0$ is an optimal point. Second, the ellipse in Fig. 3(b) shows the contour corresponding to $1 - \bar{F} = 10^{-3}$, indicating that such high-fidelity gate operation can be achieved even for the relative errors as large as $|\delta_0| = 0.01$ or $|\delta_1| = 0.05$. In particular, this gate operation is robust for the error δ_1, namely, the error in the counterpulse.

B. Simulation results for R_{zz}

For R_{zz} we obtain results that are qualitatively similar to those of R_z, which may be because for one KPO the other acts like a single-photon drive as in R_z. Figure 4 shows that, with analytic waveforms, the minimum gate time satisfying
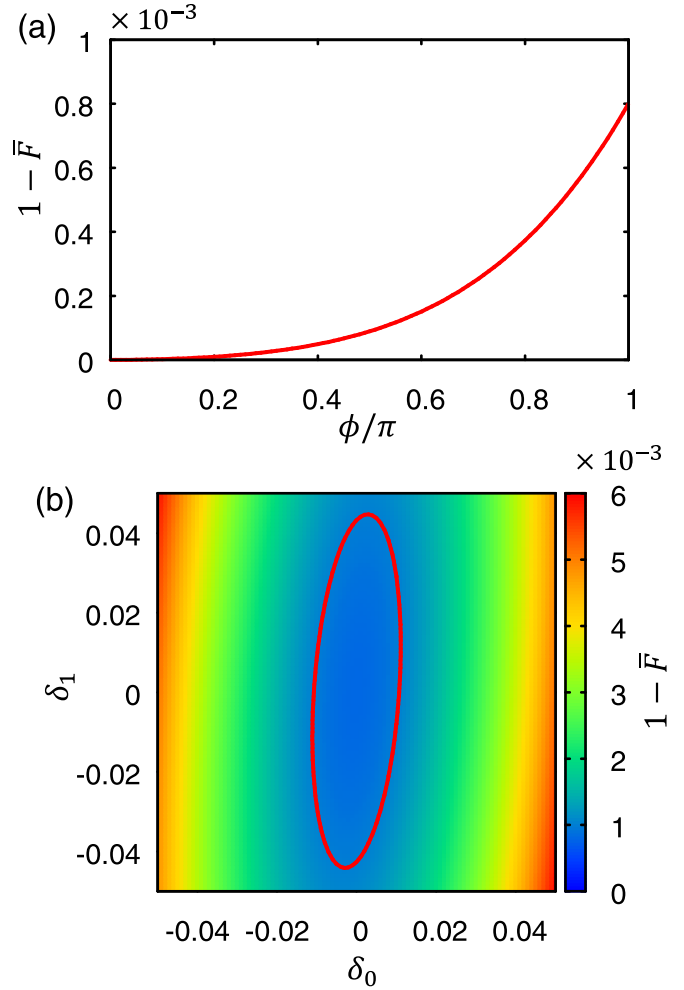

FIG. 3. (a) Average infidelity for $R_z(\phi)$ obtained by $\lambda g_j(t)$ with $g_j(t)$ shown in Fig. 1(b), which are optimized to $R_z(\pi)$, and a time-independent scaling parameter $0 \leqslant \lambda \leqslant 1$. (b) Average infidelity for $R_z(\pi)$ obtained by $(1 + \delta_j)g_j(t)$ with the optimized $g_j(t)$ and relative errors δ_j. The line indicates $1 - \bar{F} = 10^{-3}$.

$1 - \bar{F} < 10^{-3}$ is $KT_{\min} = 1.2$ and 0.6 without and with the counterterm, respectively. With the numerical optimization, the corresponding $KT_{\min}$ are 0.8 and 0.2. Thus, the numerically optimized gate operation with the counterterm provides a speedup by 6.0 times compared with the original analytic waveform without the counterterm. [See Appendix E for the optimized waveforms of $g_j(t)$, the continuous $R_{zz}(\Theta)$, and the optimality.]

C. Simulation results for R_x

Although R_x differs from R_z and R_{zz} in that R_x transfers a part of population between the two computational basis states while R_z and R_{zz} do not, the proposed method is also effective for R_x. Figure 5 shows $1 - \bar{F}$ for $R_x(\pi/2)$ as a function of KT. With analytic waveforms, the $KT_{\min}$ are 2.6 both with and without the counterterm. With the numerical optimization, the $KT_{\min}$ are 1.7 and 0.6 without and with the counterterm, respectively, which means that our approach can achieve a 4.3 times faster gate operation than that with the original analytic
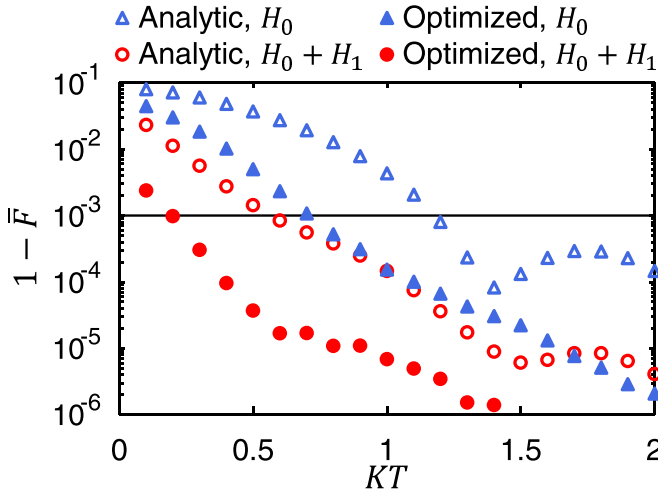
FIG. 4. Plot of average infidelities for $R_{zz}(\pi/2)$ as a function of gate time.

waveform without the counterterm. However, we find that for $KT \leqslant 0.9$, the maximum value of $|g_j(t)|/K$ can be larger than 50, which might be infeasible because the rotating-wave approximation would no longer be valid [50]. Thus, in the following, we examine optimized $g_j(t)$ at $KT = 1$, which is an acceleration by 2.6 times compared with the analytic waveform without the counterterm. Then the pulse amplitudes with $|g_j(t)|/K < 20$ are obtained as shown in Fig. 6(a).

We find that the states largely change during the optimized R_x as follows. Figures 6(b) and 6(c) show the time evolutions of the mean photon numbers $\langle\psi|a^\dagger a|\psi\rangle$ and the populations in the qubit space $\langle\psi|P|\psi\rangle$, respectively. The mean photon numbers become small during the operation, because the large detuning suppresses the oscillation of the KPO. Also, the populations in the qubit space decrease from 1, indicating that the state is altered from the superposition of the coherent states. (See Appendix F for the Wigner function during the optimized R_x.) Since the populations outside the qubit space can eventually become leakage errors, the errors in this R_x might
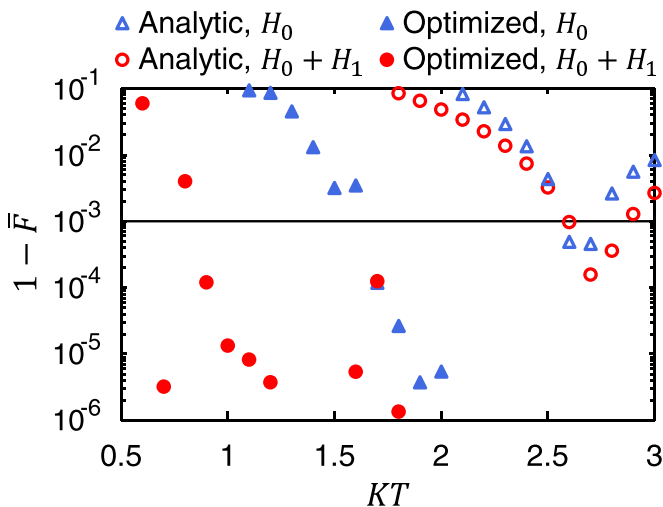

FIG. 5. Plot of average infidelities for $R_x(\pi/2)$ as a function of gate time.
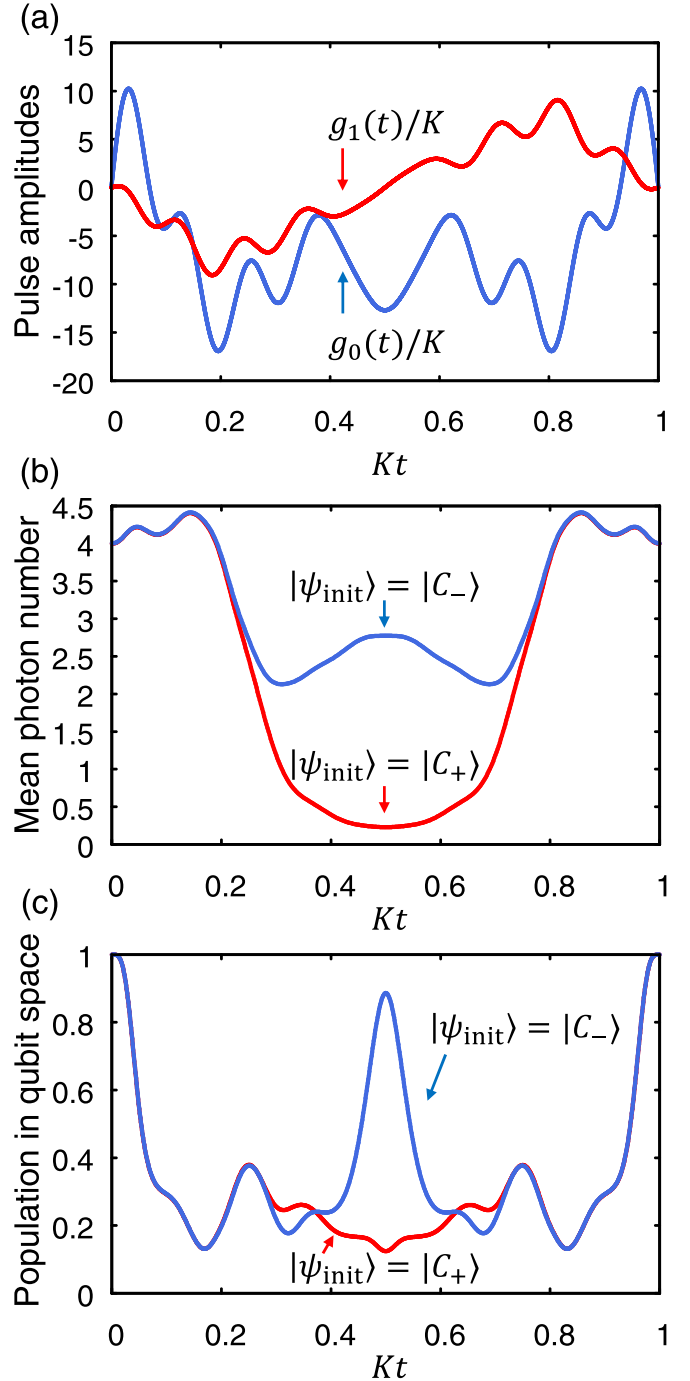

FIG. 6. (a) Waveforms of the amplitudes of $g_j(t)$ for $R_x(\pi/2)$ with a counterterm, optimized numerically for $KT = 1$. (b) Mean photon number and (c) population in the qubit space during the optimized $R_x(\pi/2)$.

be more sensitive to the gate times and optimized waveforms than in R_z and R_{zz}, causing the irregular dependence of $1 - \bar{F}$ on KT in Fig. 5.

As mentioned in Sec. III A, we find that $R_x(\theta)$ for continuous θ is not obtained by $\lambda g_j(t)$ with the optimized $g_j(t)$ for $\theta = \pi/2$. This might be because the states largely change from the two coherent states during the optimized $R_x(\pi/2)$ as
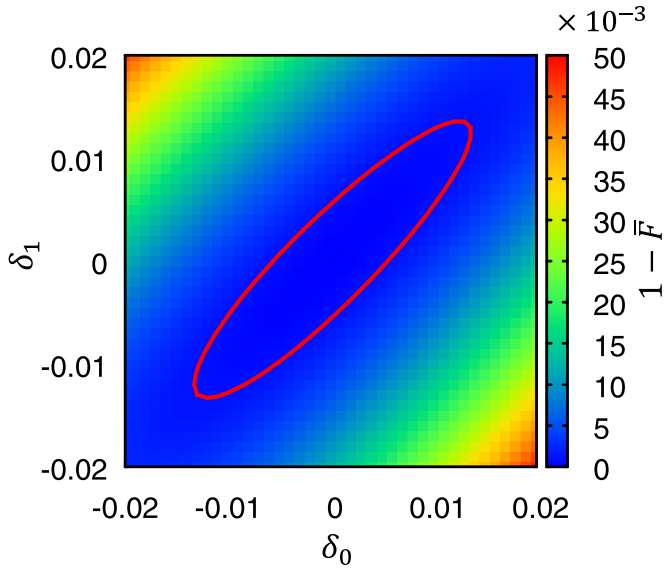
FIG. 7. Average infidelity for $R_x(\pi/2)$ obtained by $(1 + \delta_j)g_j(t)$ with the optimized $g_j(t)$ in Fig. 6(a). The line indicates $1 - \bar{F} = 10^{-3}$.

indicated above [Figs. 6(b) and 6(c)], unlike R_z and R_{zz} (see Appendix B 3).

The optimality and robustness of the optimized $g_j(t)$ are again evaluated by the gate operation by $(1 + \delta_j)g_j(t)$. Figure 7 shows the average infidelity as a function of δ_j, indicating that the optimality and robustness hold. Compared with R_z and R_{zz}, the average infidelity for R_x shows larger correlation between δ_0 and δ_1, that is, the optimized R_x is more robust against the relative errors with $\delta_0 \simeq \delta_1$. This result suggests that the counterpulse $g_1(t)$ plays a more important role in R_x than in the others.

D. Effect of single-photon loss

Finally, we evaluate errors in the presence of single-photon loss, which we choose as a representative of decoherence sources in KPOs. We solve the master equation for a density operator ρ,

$$\dot{\rho} = -i[H(t), \rho] + \mathcal{L}[\rho], \qquad (28)$$

$$\mathcal{L}[\rho] = \frac{\kappa}{2}(2a\rho a^\dagger - a^\dagger a\rho - \rho a^\dagger a) \quad \text{for } R_z, R_x, \quad (29)$$

$$\mathcal{L}[\rho] = \frac{\kappa}{2} \sum_{i=1,2}(2a_i\rho a_i^\dagger - a_i^\dagger a_i\rho - \rho a_i^\dagger a_i) \quad \text{for } R_{zz}, \quad (30)$$

where $[O_1, O_2] = O_1 O_2 - O_2 O_1$ is the commutation relation for operators and κ is the loss rate. The $H(t)$ are given in Eqs. (22) and (23) and the optimized $g_j(t)$ are used. Here we evaluate an average gate fidelity calculated with a finite number of initial states $\bar{F}_{\text{loss}}$, which is defined by Eq. (C3) in Appendix C.

Figure 8 shows $1 - \bar{F}_{\text{loss}}$ as a function of the loss rate. For all of R_z, R_{zz}, and R_x, the errors can be suppressed below $1 - \bar{F}_{\text{loss}} < 10^{-3}$ for a loss rate as large as $\kappa/K \lesssim 3 \times 10^{-4}$, except for R_z with $KT = 0.5$, R_{zz} with $KT = 0.2$, and R_x with $KT = 2$. These results are explained as follows. When
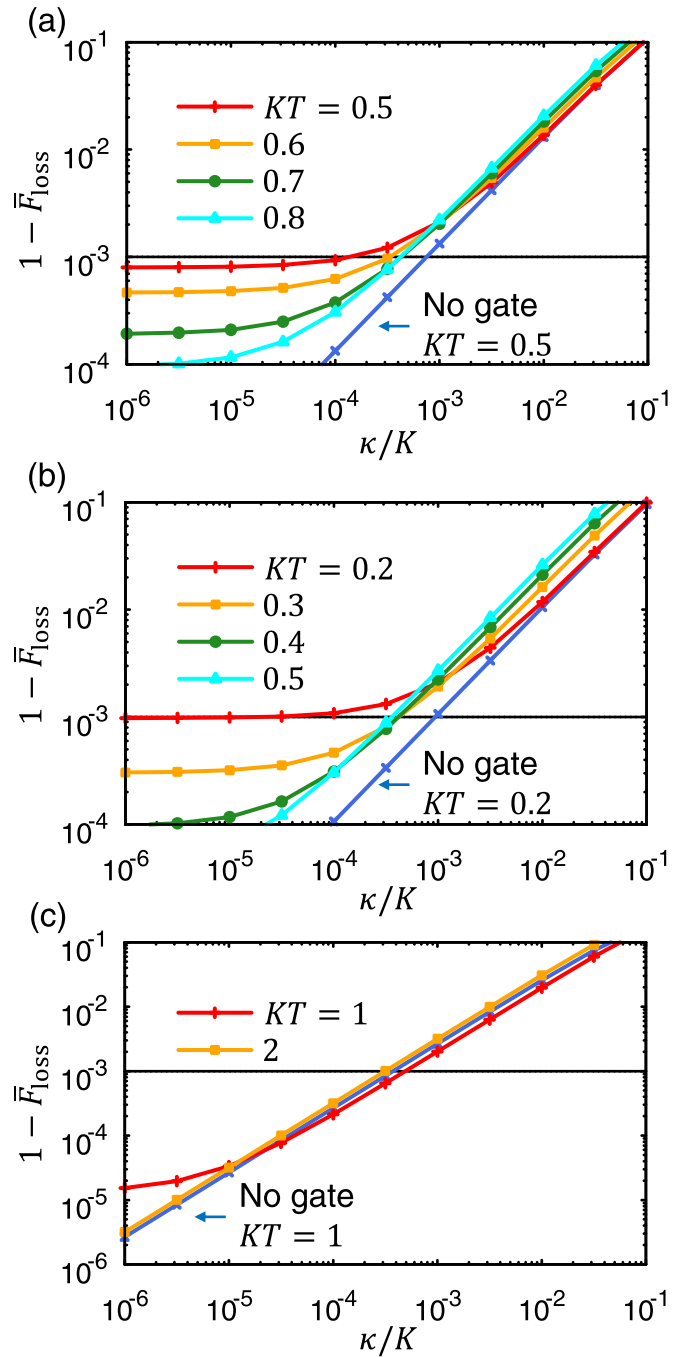

FIG. 8. Plot of average infidelities as a function of the loss rate for (a) $R_z(\pi)$, (b) $R_{zz}(\pi/2)$, and (c) $R_x(\pi/2)$, where optimized $g_j(t)$ are used. No gate means $g_j(t) = 0$ and its ideal operation is no rotation. The horizontal line indicates $1 - \bar{F}_{\text{loss}} = 10^{-3}$.

the gate times KT are too short, the leakage errors are large, which dominate the errors for the small loss rate κ/K. When the KT are too long, the single-photon loss causes large dephasing errors [9] [cf. Eq. (C5)]. The dephasing errors are the main causes of the errors for large κ/K. Indeed, the $1 - \bar{F}_{\text{loss}}$ with and without the gate operations overlap for the same KT, especially for R_z and R_{zz} in Figs. 8(a) and 8(b). For these reasons, at $\kappa/K = 3 \times 10^{-4}$, the $1 - \bar{F}_{\text{loss}}$ are the smallest at intermediate KT, achieving $1 - \bar{F}_{\text{loss}} < 10^{-3}$ as above.

In Fig. 8(c), for large κ/K, R_x gives smaller $1 - \bar{F}_{\text{loss}}$ than no gate operation, because the mean photon number is decreased during R_x as shown in Fig. 6(b) and the effect of single-photon loss becomes smaller [cf. Eq. (C5)].

IV. SUMMARY

We have shown that adiabatic elementary gates for universal quantum computation with KPO qubits can be accelerated by utilizing counterterms derived from STAs and numerically optimizing the pulse shapes for them. The optimized gate operations are feasible in experiments with, specifically, superconducting circuits. We thus expect that the proposed methods are useful for quantum computers with KPOs.

The resulting counterterms for R_z and R_{zz} are a single-photon drive and a two-mode squeezing, respectively. Related results have been reached with the DRAG technique in Ref. [13], where R_z and R_{zz} are studied as a part of the bias-preserving gates. However, the pulse shapes are analytically determined in Ref. [13]. In our work the pulse shapes are fully optimized numerically.

In this work we have clarified a counterterm for R_x. We have found that the counterterm can be approximated by a two-photon drive. Using this counterterm, we obtained a gate time for $R_x(\pi/2)$ as short as $KT = 1$. This gate time is better than that of the fastest $R_x(\pi/2)$ reported, $KT = \pi/2$, which was experimentally implemented with sharply turning off the parametric drive for this time interval [19,86].

In this work we have fixed the amplitude of the parametric drive p to $4K$ for the reasons mentioned in Sec. III. However, the proposed methods can be applied to other p in principle, and then p can be further optimized as follows. Rotations R_z and R_{zz} will become faster with a larger p, because the larger p stabilizes the two coherent states more and thus larger-amplitude pulses can be used for the gate operations [13]. Rotation R_x will be the fastest at some intermediate p, because a too large p makes the population transfer between the two coherent states difficult [73]. Furthermore, a time-dependent p can be utilized for nonadiabatic R_x, as mentioned above [19].

Although we have assumed the realistic pulse shapes and optimized them, the pulse shapes could be determined with other methods such as quantum optimal controls [87,88]. Such optimizations, including p, are left for future work.

APPENDIX A: APPROXIMATE COUNTERTERMS

We start from an exact counterterm $H_1(t)$ given by [78,80]

$$H_1(t) = i \sum_k [|\dot{E}_k(t)\rangle\langle E_k(t)|$$
$$- \langle E_k(t)|\dot{E}_k(t)\rangle |E_k(t)\rangle\langle E_k(t)|], \quad \text{(A1)}$$

where $|E_k(t)\rangle$ is the kth eigenstate of $H_0(t)$ with its eigenvalue $E_k(t)$,

$$H_0(t)|E_k(t)\rangle = E_k(t)|E_k(t)\rangle. \quad \text{(A2)}$$

The first term on the right-hand side of Eq. (A1) cancels transitions between different $|E_k(t)\rangle$, while the second term corrects phase factors. We ignore the second term because we find that $\langle E_k(t)|\dot{E}_k(t)\rangle$ vanishes in the approximation below. We then express $H_1(t)$ in an explicitly Hermitian form using the time derivative of $\sum_k |E_k(t)\rangle\langle E_k(t)| = I$ (I is the identity operator) as

$$H_1(t) \simeq \frac{i}{2} \sum_k [|\dot{E}_k(t)\rangle\langle E_k(t)| - |E_k(t)\rangle\langle \dot{E}_k(t)|]. \quad \text{(A3)}$$

To cancel transitions from a qubit space, we restrict the summation to k for computational basis states.

From Eq. (A3) we derive approximate counterterms for KPOs. We approximate $|E_k(t)\rangle$ corresponding to the qubit states by a variational method using a coherent state $|\beta\rangle$ as a trial state [28]. Its amplitude β is determined by seeking an extremum with

$$\frac{\partial}{\partial \beta} \langle \beta|H_0(t)|\beta\rangle = 0. \quad \text{(A4)}$$

1. Approximate counterterm for R_z

For R_z, we approximately solve Eq. (A4) by assuming $|g_0(t)/2K\alpha^3| \ll 1$ and obtain the expression for the qubit states

$$|E_0(t)\rangle \simeq \left|\alpha + \frac{g_0(t)}{2K\alpha^2}\right\rangle, \quad \text{(A5)}$$

$$|E_1(t)\rangle \simeq \left|-\alpha + \frac{g_0(t)}{2K\alpha^2}\right\rangle, \quad \text{(A6)}$$

where $\alpha = \sqrt{p/K}$. For real $\beta(t)$,

$$|\dot{\beta}(t)\rangle = \dot{\beta}(t)[a^\dagger - \beta(t)]|\beta(t)\rangle \quad \text{(A7)}$$

holds. Equation (A3) can then give Eq. (14) as

$$H_1(t) \simeq \frac{ig_0(t)}{4K\alpha^2}[a^\dagger P(t) - P(t)a] \quad \text{(A8)}$$

$$\simeq \frac{ig_0(t)}{4K\alpha^2}(a^\dagger - a), \quad \text{(A9)}$$

where $P(t) = |E_0(t)\rangle\langle E_0(t)| + |E_1(t)\rangle\langle E_1(t)|$ is a projector onto the qubit space. In Eq. (A9) $P(t)$ is ignored because the difference between Eqs. (A8) and (A9) is proportional to $a^\dagger[I - P(t)] - [I - P(t)]a$, which has matrix elements mainly between states outside the qubit space and therefore is negligible. As mentioned above, $\langle E_k(t)|\dot{E}_k(t)\rangle$ vanishes, because a real $\beta(t)$ gives $\langle \beta(t)|a^\dagger = \langle \beta(t)|\beta(t)$ and then Eq. (A7) leads to $\langle \beta(t)|\dot{\beta}(t)\rangle = 0$.

2. Approximate counterterm for R_{zz}

The following derivation is valid for both the beam-splitter coupling in Eq. (12) and the two-mode squeezing in Eq. (13). From Eq. (A4), when $|g_0(t)/2K\alpha^2| \ll 1$, the qubit states are

approximately given by

$$|E_{s_1 s_2}(t)\rangle \simeq \left| s_1 \alpha + \frac{s_2 g_0(t)}{2K\alpha} \right\rangle \left| s_2 \alpha + \frac{s_1 g_0(t)}{2K\alpha} \right\rangle, \quad (A10)$$

where the states are labeled with $s_i = \pm 1$ for $i = 1, 2$. Equation (A3) then becomes

$$H_1(t) \simeq \frac{i\dot{g}_0(t)}{4K\alpha} \sum_{s_1=\pm 1, s_2=\pm 1} [(s_2 a_1^\dagger + s_1 a_2^\dagger)|E_{s_1 s_2}(t)\rangle\langle E_{s_1 s_2}(t)|$$
$$- |E_{s_1 s_2}(t)\rangle\langle E_{s_1 s_2}(t)|(s_2 a_1 + s_1 a_2)]. \quad (A11)$$

Using $\sum_{s_1 s_2} s_i |E_{s_1 s_2}(t)\rangle\langle E_{s_1 s_2}(t)| \simeq P(t) a_i P(t)/\alpha = P(t) a_i^\dagger P(t)/\alpha$ with $P(t) = \sum_{s_1 s_2} |E_{s_1 s_2}(t)\rangle\langle E_{s_1 s_2}(t)|$ and ignoring $P(t)$ in a similar manner to R_z, we obtain approximate $H_1(t)$ as

$$H_1(t) \simeq \frac{i\dot{g}_0(t)}{2K\alpha^2}(a_1^\dagger a_2^\dagger - a_1 a_2), \quad (A12)$$

which is a two-mode squeezing Hamiltonian. Note that Eq. (A11) does not yield beam-splitter coupling, because if we choose the approximation of $\sum_{s_1 s_2} s_i |E_{s_1 s_2}(t)\rangle\langle E_{s_1 s_2}(t)|$ such that $a_1^\dagger a_2$ and $a_2^\dagger a_1$ appear, then $H_1(t)$ becomes zero.

3. Approximate counterterm for R_x

For R_x, Eq. (A4) gives $\beta(t) = \sqrt{[p + g_0(t)]/K}$ and the eigenstates can be approximated by

$$|E_0(t)\rangle \simeq \frac{1}{\sqrt{2}}[|\beta(t)\rangle + |-\beta(t)\rangle], \quad (A13)$$

$$|E_1(t)\rangle \simeq \frac{1}{\sqrt{2}}[|\beta(t)\rangle - |-\beta(t)\rangle], \quad (A14)$$

where $|\langle\beta(t)| - \beta(t)\rangle| \ll 1$ is assumed. The counterterm in Eq. (A3) becomes

$$H_1(t) \simeq \frac{i\dot{g}_0(t)}{4K\beta(t)}[a^\dagger Z(t) - Z(t)a], \quad (A15)$$

where $Z(t) = |\beta(t)\rangle\langle\beta(t)| - |-\beta(t)\rangle\langle-\beta(t)|$ is a Z operator in the qubit space. Using $Z(t) = P(t) a P(t)/\beta(t) = P(t) a^\dagger P(t)/\beta(t)$, ignoring $P(t)$ similarly to R_{zz}, and assuming $|g_0(t)/p| \ll 1$, we obtain nonzero Hermitian $H_1(t)$ as follows:

$$H_1(t) \simeq \frac{i\dot{g}_0(t)}{4K\alpha^2}(a^{\dagger 2} - a^2). \quad (A16)$$

APPENDIX B: PROPERTIES OF COUNTERTERMS

The exact counterterm in Eq. (A1) can be rewritten by using time derivative of the eigenvalue equation in Eq. (A2) as [78,80]

$$H_1(t) = i\dot{g}_0(t) \sum_{k\neq m} \frac{|E_k(t)\rangle\langle E_k(t)|A_0|E_m(t)\rangle\langle E_m(t)|}{E_m(t) - E_k(t)}, \quad (B1)$$

where the $H_0(t)$ in Eqs. (8) and (11) have been assumed.

1. Matrix elements

The matrix elements for $k \neq m$ are

$$\langle E_k(t)|H_1(t)|E_m(t)\rangle = i\dot{g}_0(t) \frac{\langle E_k(t)|A_0|E_m(t)\rangle}{E_m(t) - E_k(t)}. \quad (B2)$$

Equation (B2) means that to cancel unwanted transitions, when the matrix elements of A_0 [and $\dot{g}_0(t)$] are nonzero, the corresponding matrix elements of a counterterm $H_1(t)$ must also be nonzero. Thus, an approximate $H_1(t)$ may be more effective when its matrix elements are more similar to those of A_0. As mentioned in Sec. II B, we think that for the above reason, $H_1(t)$ with the two-mode squeezing in Eq. (16) works better for A_0 with the two-mode squeezing in Eq. (13) than A_0 with the beam-splitter coupling in Eq. (12).

Also, to have nonzero matrix elements in common, $H_1(t)$ must have the same symmetries as A_0. On the other hand, as mentioned in Sec. II B, the counterterm with the beam-splitter coupling in Eq. (17) has permutation symmetry different from A_0 in Eqs. (12) and (13), that is, the interchange of KPO1 and KPO2 leads to a sign change in Eq. (17) but not in A_0. Thus, the counterterm in Eq. (17) may not be effective.

2. Time-reversal symmetry

Based on Eq. (B1), here we consider the symmetry of $H_1(t)$ with respect to a time reversal $t \to T - t$. When $g_0(t)$ and hence $H_0(t)$ are symmetric, namely, $H_0(T - t) = H_0(t)$, the eigenvalue equation (A2) indicates that $E_k(t)$ and $|E_k(t)\rangle$ are also symmetric, that is, they can be chosen to be $E_k(T - t) = E_k(t)$ and $|E_k(T - t)\rangle = |E_k(t)\rangle$. Also, when $g_0(t)$ is symmetric, $\dot{g}_0(t)$ is antisymmetric, $\dot{g}_0(T - t) = -\dot{g}_0(t)$. Equation (B1) then indicates that symmetric $g_0(t)$ yields antisymmetric $H_1(t)$. We thus use antisymmetric $g_1(t)$ in Eq. (25) for numerical optimization.

3. One-parameter continuous gate with a counterterm

Equation (B1) indicates that a scaled $\lambda g_0(t)$ does not necessary scale $H_1(t)$ to $\lambda H_1(t)$, because $H_1(t)$ depends on $g_0(t)$ through $|E_k(t)\rangle$ and $E_k(t)$. If the dependence of $|E_k(t)\rangle$ and $E_k(t)$ on $g_0(t)$ is negligible, such a scaling holds. We think that this property is related to the one-parameter continuous gates with the counterterms for R_z and R_{zz} shown in Figs. 3(a) and 9(b). Also, as mentioned in Sec. III C, since R_x largely changes the state during the gate operation, the one-parameter continuous gate would not work.

APPENDIX C: AVERAGE GATE FIDELITIES

When dissipation is not included, we calculate a gate fidelity averaged over all initial states in a qubit space by [84]

$$\bar{F} = \frac{1}{d(d+1)}[|\text{tr}(U_0^\dagger U)|^2 + \text{tr}(UU^\dagger)], \quad (C1)$$

where $d = 2, 4$ is the dimension of the qubit space for a single- and a two-qubit gate, respectively, $U_0 = R_z, R_x, R_{zz}$ is an ideal gate operation, and U is a time-evolution operator projected onto the qubit space. For a single-qubit gate, U can be given by

$$U = \begin{pmatrix} \langle \tilde{0}|\psi_0\rangle & \langle \tilde{0}|\psi_1\rangle \\ \langle \tilde{1}|\psi_0\rangle & \langle \tilde{1}|\psi_1\rangle \end{pmatrix}, \quad (C2)$$

where $|\psi_0\rangle$ and $|\psi_1\rangle$ are states after time evolution for the gate time T calculated with the Schrödinger equation (26) with the initial states $|\tilde{0}\rangle$ and $|\tilde{1}\rangle$, respectively. For a two-qubit gate U can be calculated similarly with the initial states $|\tilde{0}\tilde{0}\rangle$, $|\tilde{0}\tilde{1}\rangle$, $|\tilde{1}\tilde{0}\rangle$, and $|\tilde{1}\tilde{1}\rangle$.

When the single-photon loss is included, we calculate the average gate fidelity

$$\bar{F}_{\text{loss}} = \frac{1}{N_{\text{init}}} \sum_{l=1}^{N_{\text{init}}} \langle \psi_{\text{init}}^{(l)} | U_0^\dagger \rho_l U_0 | \psi_{\text{init}}^{(l)} \rangle, \tag{C3}$$

where $|\psi_{\text{init}}^{(l)}\rangle$ is an initial state and ρ_l is the density operator of a final state calculated from the initial state $|\psi_{\text{init}}^{(l)}\rangle$ with the master equation (28). Here N_{init} is the number of initial states. For a single-qubit gate, we choose the following six initial states for $l = 1, 2, \ldots, 6$:

$$|\psi_{\text{init}}^{(l)}\rangle = \begin{pmatrix} 1 \\ 0 \end{pmatrix}, \quad \begin{pmatrix} 0 \\ 1 \end{pmatrix}, \quad \frac{1}{\sqrt{2}} \begin{pmatrix} 1 \\ 1 \end{pmatrix}, \quad \frac{1}{\sqrt{2}} \begin{pmatrix} 1 \\ -1 \end{pmatrix},$$

$$\frac{1}{\sqrt{2}} \begin{pmatrix} 1 \\ i \end{pmatrix}, \quad \frac{1}{\sqrt{2}} \begin{pmatrix} 1 \\ -i \end{pmatrix}. \tag{C4}$$

For a two-qubit gate, we use the 36 initial states given by $|\psi_{\text{init}}^{(l)}\rangle |\psi_{\text{init}}^{(l')}\rangle$ with $l, l' = 1, 2, \ldots, 6$. We numerically find that $\bar{F}_{\text{loss}}$ is in good agreement with $\bar{F}$ in the absence of the single-photon loss. The average infidelity due to the single-photon loss alone can be approximated well by [9,75]

$$1 - \bar{F}_{\text{loss}} \simeq \frac{1}{3}(1 - e^{-2\alpha^2 \kappa T}), \tag{C5}$$

per KPO for the large mean photon number $\alpha^2 \gg 1$.

APPENDIX D: WAVEFORMS OF PULSE AMPLITUDES

1. Waveforms for R_z

For R_z we use the following waveforms: (a) analytic waveforms [8] without the counterterm

$$g_0(t) = \frac{\pi\phi}{8T\alpha} \sin\frac{\pi t}{T}, \tag{D1}$$

$$g_1(t) = 0; \tag{D2}$$

(b) analytic waveforms with the counterterm in Eq. (14),

$$g_0(t) = \frac{\pi\phi}{8T\alpha} \sin\frac{\pi t}{T}, \tag{D3}$$

$$g_1(t) = \frac{\dot{g}_0(t)}{4K\alpha^2}; \tag{D4}$$

(c) numerically optimized waveforms in Eq. (24) without the counterterm, where the initial $g_{j,n}$ are

$$g_{0,2} = \frac{\phi}{2T\alpha}, \tag{D5}$$

$$g_{j,n} = 0 \quad \text{for the others}; \tag{D6}$$

and (d) numerically optimized waveforms in Eqs. (24) and (25) with the counterterm, where the initial $g_{j,n}$ are [cf. Eq. (D4)]

$$g_{0,2} = \frac{\phi}{2T\alpha}, \tag{D7}$$

$$g_{1,1} = \frac{\pi g_{0,2}}{4KT\alpha^2}, \tag{D8}$$

$$g_{j,n} = 0 \quad \text{for the others}. \tag{D9}$$

2. Waveforms for R_{zz}

For R_{zz} we use the following waveforms: (a) analytic waveforms [8] without the counterterm,

$$g_0(t) = \frac{\pi\Theta}{8T\alpha^2} \sin\frac{\pi t}{T}, \tag{D10}$$

$$g_1(t) = 0; \tag{D11}$$

(b) analytic waveforms with the counterterm in Eq. (16),

$$g_0(t) = \frac{\pi\Theta}{8T\alpha^2} \sin\frac{\pi t}{T}, \tag{D12}$$

$$g_1(t) = \frac{\dot{g}_0(t)}{2K\alpha^2}; \tag{D13}$$

(c) numerically optimized waveforms in Eq. (24) without the counterterm, where the initial $g_{j,n}$ are

$$g_{0,2} = \frac{\Theta}{2T\alpha^2}, \tag{D14}$$

$$g_{j,n} = 0 \text{ for the others}; \tag{D15}$$

and (d) numerically optimized waveforms in Eqs. (24) and (25) with the counterterm, where the initial $g_{j,n}$ are [cf. Eq. (D13)]

$$g_{0,2} = \frac{\Theta}{2T\alpha^2}, \tag{D16}$$

$$g_{1,1} = \frac{\pi g_{0,2}}{2KT\alpha^2}, \tag{D17}$$

$$g_{j,n} = 0 \quad \text{for the others}. \tag{D18}$$

3. Waveforms for R_x

For R_x we use the following waveforms: (a) analytic waveforms [8] without the counterterm, where the Δ is determined by maximizing $\bar{F}$,

$$g_0(t) = \frac{\Delta}{2}\left(1 - \cos\frac{2\pi t}{T}\right), \tag{D19}$$

$$g_1(t) = 0; \tag{D20}$$

(b) analytic waveforms with the counterterm in Eq. (15), where Δ_{count} is determined as above,

$$g_0(t) = \frac{\Delta_{\text{count}}}{2}\left(1 - \cos\frac{2\pi t}{T}\right), \tag{D21}$$

$$g_1(t) = \frac{\dot{g}_0(t)}{4K\alpha^2}; \tag{D22}$$

FIG. 10. Wigner functions during $R_x(\pi/2)$ with the optimized $g_j(t)$ in Fig. 6(a). (a), (d) $Kt = 0.2$, (b), (e) $Kt = 0.5$, and (c), (f) $Kt = 0.8$. The initial states are [(a)–(c)] $|C_+\rangle$ and [(d)–(f)] $|C_-\rangle$.

and (d) numerically optimized waveforms in Eqs. (24) and (25) with the counterterm, where Δ_{count} is determined for the analytic waveforms in Eq. (D21) and the initial $g_{j,n}$ are [cf. Eq. (D22)]

$$g_{0,2} = \Delta_{count}, \tag{D25}$$

$$g_{1,1} = \frac{\pi g_{0,2}}{4KT\alpha^2}, \tag{D26}$$

$$g_{j,n} = 0 \quad \text{for the others.} \tag{D27}$$

APPENDIX E: SIMULATION RESULTS FOR R_{zz}

Optimized waveforms $g_j(t)$ with the counterterm at $KT_{min} = 0.2$ are shown in Fig. 9(a). Figure 9(b) shows that these optimized $g_j(t)$ can be used for continuous $R_{zz}(\Theta)$ by $\lambda g_j(t)$ with the time-independent scaling parameter λ as in the case of $R_z(\phi)$. Also, the optimality and robustness of $R_{zz}(\pi/2)$ are evaluated with $(1 + \delta_j)g_j(t)$. Figure 9(c) shows that the gradient of $1 - \bar{F}$ is zero at $\delta_0 = \delta_1 = 0$, indicating its optimality.

APPENDIX F: WIGNER FUNCTION DURING R_x

Figure 10 shows the Wigner function during the optimized R_x in Fig. 6(a). Figure 10(b) shows that for $|\psi_{init}\rangle = |C_+\rangle$ the intermediate state looks like a vacuum state, which agrees with the small mean photon number in Fig. 6(b). The vacuum state may be realized because the large $|g_0(t)|/K$ suppresses the oscillation of the KPO. On the other hand, Fig. 10(e) shows that for $|\psi_{init}\rangle = |C_-\rangle$ the intermediate state resembles $|C_-\rangle$, which is consistent with the large population in the qubit space for $Kt = 0.5$ in Fig. 6(c).
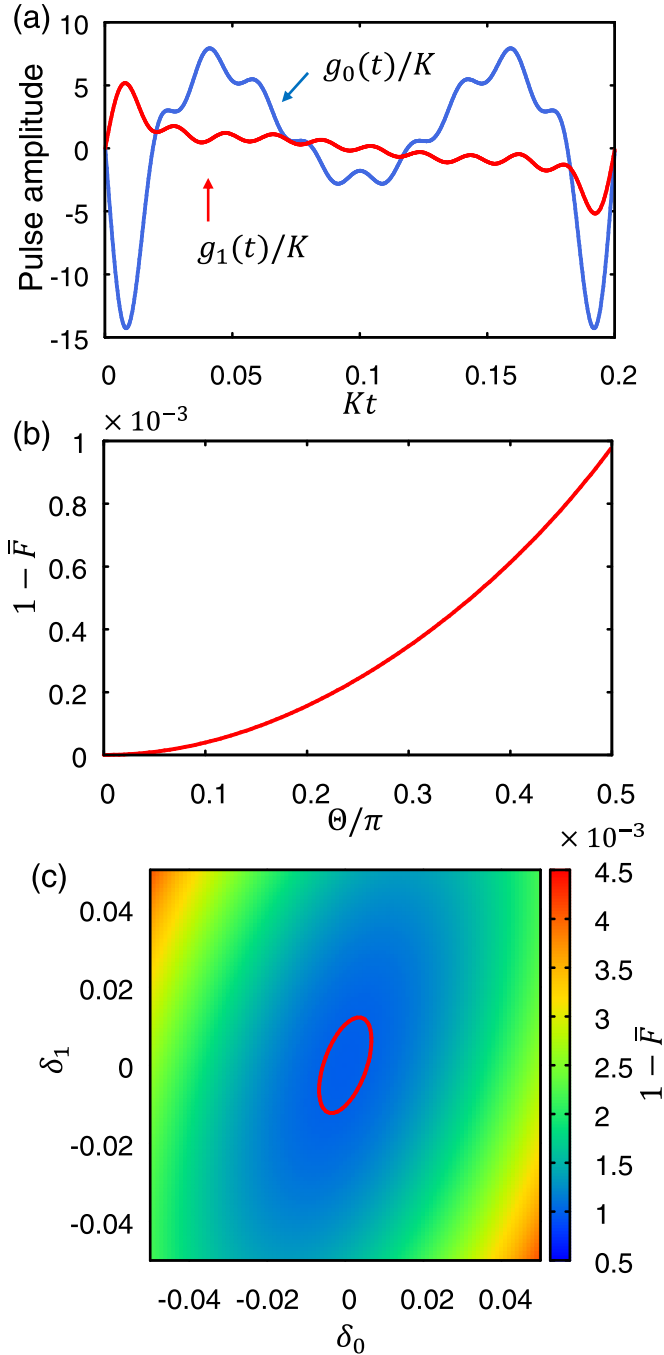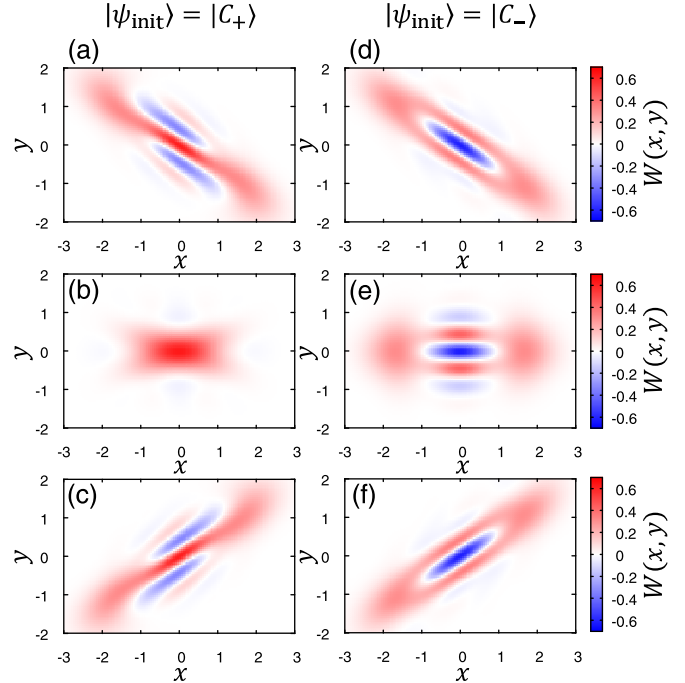

FIG. 9. (a) Waveforms of $g_j(t)$ for $R_{zz}(\pi/2)$ with a counterterm, optimized numerically for $KT_{min} = 0.2$. (b) Average infidelity for $R_{zz}(\Theta)$ obtained by $\lambda g_j(t)$ with the optimized $g_j(t)$ in (a). (c) Average infidelity for $R_{zz}(\pi/2)$ obtained by $(1 + \delta_j)g_j(t)$ with the optimized $g_j(t)$. The line indicates $1 - \bar{F} = 10^{-3}$.

(c) numerically optimized waveforms in Eq. (24) without the counterterm, where Δ is determined for the analytic waveforms in Eq. (D19) and the initial $g_{j,n}$ are

$$g_{0,2} = \Delta, \tag{D23}$$

$$g_{j,n} = 0 \quad \text{for the others;} \tag{D24}$$

[1] P. T. Cochrane, G. J. Milburn, and W. J. Munro, Macroscopically distinct quantum-superposition states as a bosonic code for amplitude damping, Phys. Rev. A **59**, 2631 (1999).

[2] M. Mirrahimi, Z. Leghtas, V. V. Albert, S. Touzard, R. J. Schoelkopf, L. Jiang, and M. H. Devoret, Dynamically protected cat-qubits: A new paradigm for universal quantum computation, New J. Phys. **16**, 045014 (2014).

[3] B. Yurke and D. Stoler, Generating quantum mechanical superpositions of macroscopically distinguishable states via amplitude dispersion, Phys. Rev. Lett. **57**, 13 (1986).

[4] S. Deléglise, I. Dotsenko, C. Sayrin, J. Bernu, M. Brune, J.-M. Raimond, and S. Haroche, Reconstruction of non-classical cavity field states with snapshots of their decoherence, Nature (London) **455**, 510 (2008).

[5] M. Wolinsky and H. J. Carmichael, Quantum noise in the parametric oscillator: From squeezed states to coherent-state superpositions, Phys. Rev. Lett. **60**, 1836 (1988).

[6] B. Wielinga and G. J. Milburn, Quantum tunneling in a Kerr medium with parametric pumping, Phys. Rev. A **48**, 2494 (1993).

[7] H. Goto, Bifurcation-based adiabatic quantum computation with a nonlinear oscillator network, Sci. Rep. **6**, 21686 (2016).

[8] H. Goto, Universal quantum computation with a nonlinear oscillator network, Phys. Rev. A **93**, 050301(R) (2016).

[9] S. Puri, S. Boutin, and A. Blais, Engineering the quantum states of light in a Kerr-nonlinear resonator by two-photon driving, npj Quantum Inf. **3**, 18 (2017).

[10] H. Goto, Quantum computation based on quantum adiabatic bifurcations of Kerr-nonlinear parametric oscillators, J. Phys. Soc. Jpn. **88**, 061015 (2019).

[11] S. E. Nigg, N. Lörch, and R. P. Tiwari, Robust quantum optimizer with full connectivity, Sci. Adv. **3**, e1602273 (2017).

[12] Z. Wang, M. Pechal, E. A. Wollack, P. Arrangoiz-Arriola, M. Gao, N. R. Lee, and A. H. Safavi-Naeini, Quantum dynamics of a few-photon parametric oscillator, Phys. Rev. X **9**, 021049 (2019).

[13] Q. Xu, J. K. Iverson, F. G. S. L. Brandão, and L. Jiang, Engineering fast bias-preserving gates on stabilized cat qubits, Phys. Rev. Res. **4**, 013082 (2022).

[14] T. Yamaji, S. Kagami, A. Yamaguchi, T. Satoh, K. Koshino, H. Goto, Z. R. Lin, Y. Nakamura, and T. Yamamoto, Spectroscopic observation of the crossover from a classical Duffing oscillator to a Kerr parametric oscillator, Phys. Rev. A **105**, 023519 (2022).

[15] S. Masuda, T. Kanao, H. Goto, Y. Matsuzaki, T. Ishikawa, and S. Kawabata, Fast tunable coupling scheme of Kerr parametric oscillators based on shortcuts to adiabaticity, Phys. Rev. Appl. **18**, 034076 (2022).

[16] S. Kwon, S. Watabe, and J.-S. Tsai, Autonomous quantum error correction in a four-photon Kerr parametric oscillator, npj Quantum Inf. **8**, 40 (2022).

[17] Z. Leghtas, S. Touzard, I. M. Pop, A. Kou, B. Vlastakis, A. Petrenko, K. M. Sliwa, A. Narla, S. Shankar, M. J. Hatridge *et al.*, Confining the state of light to a quantum manifold by engineered two-photon loss, Science **347**, 853 (2015).

[18] R. Lescanne, M. Villiers, T. Peronnin, A. Sarlette, M. Delbecq, B. Huard, T. Kontos, M. Mirrahimi, and Z. Leghtas, Exponential suppression of bit-flips in a qubit encoded in an oscillator, Nat. Phys. **16**, 509 (2020).

[19] A. Grimm, N. E. Frattini, S. Puri, S. O. Mundhada, S. Touzard, M. Mirrahimi, S. M. Girvin, S. Shankar, and M. H. Devoret, Stabilization and operation of a Kerr-cat qubit, Nature (London) **584**, 205 (2020).

[20] G. J. Milburn, Coherence and chaos in a quantum optical system, Phys. Rev. A **41**, 6567(R) (1990).

[21] G. J. Milburn and C. A. Holmes, Quantum coherence and classical chaos in a pulsed parametric oscillator with a Kerr nonlinearity, Phys. Rev. A **44**, 4704 (1991).

[22] H. Goto and T. Kanao, Chaos in coupled Kerr-nonlinear parametric oscillators, Phys. Rev. Res. **3**, 043196 (2021).

[23] S. Puri, C. K. Andersen, A. L. Grimsmo, and A. Blais, Quantum annealing with all-to-all connected nonlinear oscillators, Nat. Commun. **8**, 15785 (2017).

[24] P. Zhao, Z. Jin, P. Xu, X. Tan, H. Yu, and Y. Yu, Two-photon driven Kerr resonator for quantum annealing with three-dimensional circuit QED, Phys. Rev. Appl. **10**, 024019 (2018).

[25] H. Goto, Z. Lin, and Y. Nakamura, Boltzmann sampling from the Ising model using quantum heating of coupled nonlinear oscillators, Sci. Rep. **8**, 7154 (2018).

[26] T. Onodera, E. Ng, and P. L. McMahon, A quantum annealer with fully programmable all-to-all coupling via Floquet engineering, npj Quantum Inf. **6**, 48 (2020).

[27] H. Goto and T. Kanao, Quantum annealing using vacuum states as effective excited states of driven systems, Commun. Phys. **3**, 235 (2020).

[28] T. Kanao and H. Goto, High-accuracy Ising machine using Kerr-nonlinear parametric oscillators with local four-body interactions, npj Quantum Inf. **7**, 18 (2021).

[29] T. Yamaji, M. Shirane, and T. Yamamoto, Development of quantum annealer using Josephson parametric oscillators, IEICE Trans. Electron. **E105-C**, 283 (2022).

[30] V. Savona, Spontaneous symmetry breaking in a quadratically driven nonlinear photonic lattice, Phys. Rev. A **96**, 033826 (2017).

[31] M. I. Dykman, C. Bruder, N. Lörch, and Y. Zhang, Interaction-induced time-symmetry breaking in driven quantum oscillators, Phys. Rev. B **98**, 195444 (2018).

[32] R. Rota, F. Minganti, C. Ciuti, and V. Savona, Quantum critical regime in a quadratically driven nonlinear photonic lattice, Phys. Rev. Lett. **122**, 110405 (2019).

[33] R. Rota and V. Savona, Simulating frustrated antiferromagnets with quadratically driven QED cavities, Phys. Rev. A **100**, 013838 (2019).

[34] M. J. Kewming, S. Shrapnel, and G. J. Milburn, Quantum correlations in the Kerr Ising model, New J. Phys. **22**, 053042 (2020).

[35] W. Verstraelen, R. Rota, V. Savona, and M. Wouters, Gaussian trajectory approach to dissipative phase transitions: The case of quadratically driven photonic lattices, Phys. Rev. Res. **2**, 022037(R) (2020).

[36] R. Miyazaki, Effective spin models of Kerr-nonlinear parametric oscillators for quantum annealing, Phys. Rev. A **105**, 062457 (2022).

[37] N. Bartolo, F. Minganti, W. Casteels, and C. Ciuti, Exact steady state of a Kerr resonator with one- and two-photon driving and dissipation: Controllable Wigner-function multimodality and dissipative phase transitions, Phys. Rev. A **94**, 033841 (2016).

[38] D. Roberts and A. A. Clerk, Driven-dissipative quantum Kerr resonators: New exact solutions, photon blockade and quantum bistability, Phys. Rev. X **10**, 021022 (2020).

[39] Y. Zhang and M. I. Dykman, Preparing quasienergy states on demand: A parametric oscillator, Phys. Rev. A **95**, 053841 (2017).

[40] H. Goto, Z. Lin, T. Yamamoto, and Y. Nakamura, On-demand generation of traveling cat states using a parametric oscillator, Phys. Rev. A **99**, 023838 (2019).

[41] R. Y. Teh, F.-X. Sun, R. E. S. Polkinghorne, Q. Y. He, Q. Gong, P. D. Drummond, and M. D. Reid, Dynamics of transient cat states in degenerate parametric oscillation with and without nonlinear Kerr interactions, Phys. Rev. A **101**, 043807 (2020).

[42] J.-J. Xue, K.-H. Yu, W.-X. Liu, X. Wang, and H.-R. Li, Fast generation of cat states in Kerr nonlinear resonators via optimal adiabatic control, New J. Phys. **24**, 053015 (2022).

[43] Y. Suzuki, S. Watabe, S. Kawabata, and S. Masuda, Measurement-based preparation of stable coherent states of a Kerr parametric oscillator, Sci. Rep. **13**, 1606 (2023).

[44] N. Bartolo, F. Minganti, J. Lolli, and C. Ciuti, Homodyne versus photon-counting quantum trajectories for dissipative Kerr resonators with two-photon driving, Eur. Phys. J. Spec. Top. **226**, 2705 (2017).

[45] S. Masuda, A. Yamaguchi, T. Yamaji, T. Yamamoto, T. Ishikawa, Y. Matsuzaki, and S. Kawabata, Theoretical study of reflection spectroscopy for superconducting quantum parametrons, New J. Phys. **23**, 093023 (2021).

[46] K. Matsumoto, A. Yamaguchi, T. Yamamoto, S. Kawabata, and Y. Matsuzaki, Spectroscopic estimation of the photon number for superconducting Kerr parametric oscillators, Jpn. J. Appl. Phys. **62**, SC1097 (2023).

[47] I. Strandberg, G. Johansson, and F. Quijandría, Wigner negativity in the steady-state output of a Kerr parametric oscillator, Phys. Rev. Res. **3**, 023041 (2021).

[48] Q.-W. Wang and S. Wu, Excited-state quantum phase transitions in Kerr nonlinear oscillators, Phys. Rev. A **102**, 063531 (2020).

[49] J. Chávez-Carlos, T. L. M. Lezama, R. G. Cortiñas, J. Venkatraman, M. H. Devoret, V. S. Batista, F. Pérez-Bernal, and L. F. Santos, Spectral kissing and its dynamical consequences in the squeeze-driven Kerr oscillator, npj Quantum Inf. **9**, 76 (2023).

[50] S. Masuda, T. Ishikawa, Y. Matsuzaki, and S. Kawabata, Controls of a superconducting quantum parametron under a strong pump field, Sci. Rep. **11**, 11459 (2021).

[51] H. Putterman, J. Iverson, Q. Xu, L. Jiang, O. Painter, F. G. S. L. Brandão, and K. Noh, Stabilizing a bosonic qubit using colored dissipation, Phys. Rev. Lett. **128**, 110502 (2022).

[52] R. Gautier, A. Sarlette, and M. Mirrahimi, Combined dissipative and Hamiltonian confinement of cat qubits, PRX Quantum **3**, 020339 (2022).

[53] D. Ruiz, R. Gautier, J. Guillaud, and M. Mirrahimi, Two-photon driven Kerr quantum oscillator with multiple spectral degeneracies, Phys. Rev. A **107**, 042407 (2023).

[54] F. Iachello, R. G. Cortiñas, F. Pérez-Bernal, and L. F. Santos, Symmetries of the squeeze-driven Kerr oscillator, J. Phys. A: Math. Theor. **56**, 495305 (2023).

[55] I. García-Mata, R. G. Cortiñas, X. Xiao, J. Chávez-Carlos, V. S. Batista, L. F. Santos, and D. A. Wisniacki, Effective versus Floquet theory for the Kerr parametric oscillator, arXiv:2309.12516.

[56] M. A. Nielsen and I. L. Chuang, *Quantum Computation and Quantum Information* (Cambridge University Press, Cambridge, UK, 2000).

[57] S. Puri, A. Grimm, P. Campagne-Ibarcq, A. Eickbusch, K. Noh, G. Roberts, L. Jiang, M. Mirrahimi, M. H. Devoret, and S. M. Girvin, Stabilized cat in a driven nonlinear cavity: A fault-tolerant error syndrome detector, Phys. Rev. X **9**, 041009 (2019).

[58] S. Puri, L. St-Jean, J. A. Gross, A. Grimm, N. E. Frattini, P. S. Iyer, A. Krishna, S. Touzard, L. Jiang, A. Blais *et al.*, Bias-preserving gates with stabilized cat qubits, Sci. Adv. **6**, eaay5901 (2020).

[59] A. S. Darmawan, B. J. Brown, A. L. Grimsmo, D. K. Tuckett, and S. Puri, Practical quantum error correction with the XZZX code and Kerr-cat qubits, PRX Quantum **2**, 030345 (2021).

[60] J. Preskill, Quantum computing in the NISQ era and beyond, Quantum **2**, 79 (2018).

[61] M. Cerezo, A. Arrasmith, R. Babbush, S. C. Benjamin, S. Endo, K. Fujii, J. R. McClean, K. Mitarai, X. Yuan, L. Cincio *et al.*, Variational quantum algorithms, Nat. Rev. Phys. **3**, 625 (2021).

[62] S. Endo, Z. Cai, S. C. Benjamin, and X. Yuan, Hybrid quantum-classical algorithms and quantum error mitigation, J. Phys. Soc. Jpn. **90**, 032001 (2021).

[63] Y. Mori, K. Nakaji, Y. Matsuzaki, and S. Kawabata, Expressive quantum supervised machine learning using Kerr-nonlinear parametric oscillators, arXiv:2305.00688.

[64] P. Vikstål, L. García-Álvarez, S. Puri, and G. Ferrini, Quantum approximate optimization algorithm with cat qubits, arXiv:2305.05556.

[65] T. Yamamoto, K. Inomata, M. Watanabe, K. Matsuba, T. Miyazaki, W. D. Oliver, Y. Nakamura, and J. S. Tsai, Flux-driven Josephson parametric amplifier, Appl. Phys. Lett. **93**, 042510 (2008).

[66] C. M. Wilson, T. Duty, M. Sandberg, F. Persson, V. Shumeiko, and P. Delsing, Photon generation in an electromagnetic cavity with a time-dependent boundary, Phys. Rev. Lett. **105**, 233907 (2010).

[67] Z. R. Lin, K. Inomata, K. Koshino, W. D. Oliver, Y. Nakamura, J. S. Tsai, and T. Yamamoto, Josephson parametric phase-locked oscillator and its application to dispersive readout of superconducting qubits, Nat. Commun. **5**, 4480 (2014).

[68] T. Yamaji, S. Masuda, A. Yamaguchi, T. Satoh, A. Morioka, Y. Igarashi, M. Shirane, and T. Yamamoto, Correlated oscillations in Kerr parametric oscillators with tunable effective coupling, Phys. Rev. Appl. **20**, 014057 (2023).

[69] N. E. Frattini, R. G. Cortiñas, J. Venkatraman, X. Xiao, Q. Su, C. U Lei, B. J. Chapman, V. R. Joshi, S. M. Girvin, R. J. Schoelkopf, S. Puri, and M. H. Devoret, The squeezed Kerr oscillator: Spectral kissing and phase-flip robustness, arXiv:2209.03934.

[70] J. Venkatraman, R. G. Cortiñas, N. E. Frattini, X. Xiao, and M. H. Devoret, A driven quantum superconducting circuit with multiple tunable degeneracies, arXiv:2211.04605.

[71] D. Iyama, T. Kamiya, S. Fujii, H. Mukai, Y. Zhou, T. Nagase, A. Tomonaga, R. Wang, J.-J. Xue, S. Watabe, S. Kwon, and J.-S. Tsai, Observation and manipulation of quantum inter-

ference in a superconducting Kerr parametric oscillator, Nat. Commun. **15**, 86 (2024).

[72] A. Yamaguchi, S. Masuda, Y. Matsuzaki, T. Yamaji, T. Satoh, A. Morioka, Y. Kawakami, Y. Igarashi, M. Shirane, and T. Yamamoto, Spectroscopy of flux-driven Kerr parametric oscillators by reflection coefficient measurement, arXiv:2309.10488.

[73] T. Kanao, S. Masuda, S. Kawabata, and H. Goto, Quantum gate for a Kerr nonlinear parametric oscillator using effective excited states, Phys. Rev. Appl. **18**, 014019 (2022).

[74] H. Chono, T. Kanao, and H. Goto, Two-qubit gate using conditional driving for highly detuned Kerr nonlinear parametric oscillators, Phys. Rev. Res. **4**, 043054 (2022).

[75] T. Aoki, T. Kanao, H. Goto, S. Kawabata, and S. Masuda, Control of the ZZ coupling between Kerr cat qubits via transmon couplers, Phys. Rev. Appl. **21**, 014030 (2024).

[76] Y.-H. Kang, Y.-H. Chen, X. Wang, J. Song, Y. Xia, A. Miranowicz, S.-B. Zheng, and F. Nori, Nonadiabatic geometric quantum computation with cat-state qubits via invariant-based reverse engineering, Phys. Rev. Res. **4**, 013233 (2022).

[77] Y.-H. Kang, Y. Xiao, Z.-C. Shi, Y. Wang, J.-Q. Yang, J. Song, and Y. Xia, Effective implementation of nonadiabatic geometric quantum gates of cat-state qubits using an auxiliary qutrit, New J. Phys. **25**, 033029 (2023).

[78] D. Guéry-Odelin, A. Ruschhaupt, A. Kiely, E. Torrontegui, S. Martínez-Garaot, and J. G. Muga, Shortcuts to adiabaticity: Concepts, methods, and applications, Rev. Mod. Phys. **91**, 045001 (2019).

[79] M. Demirplak and S. A. Rice, Adiabatic population transfer with control fields, J. Phys. Chem. A **107**, 9937 (2003).

[80] M. V. Berry, Transitionless quantum driving, J. Phys. A: Math. Theor. **42**, 365303 (2009).

[81] T. Opatrný and K. Mølmer, Partial suppression of nonadiabatic transitions, New J. Phys. **16**, 015025 (2014).

[82] J. M. Martinis and M. R. Geller, Fast adiabatic qubit gates using only σ_z control, Phys. Rev. A **90**, 022307 (2014).

[83] M. A. Nielsen, A simple formula for the average gate fidelity of a quantum dynamical operation, Phys. Lett. A **303**, 249 (2002).

[84] L. H. Pedersen, N. M. Møller, and K. Mølmer, Fidelity of quantum operations, Phys. Lett. A **367**, 47 (2007).

[85] U. Leonhardt, *Measuring the Quantum State of Light* (Cambridge University Press, Cambridge, UK, 1997).

[86] G. Kirchmair, B. Vlastakis, Z. Leghtas, S. E. Nigg, H. Paik, E. Ginossar, M. Mirrahimi, L. Frunzio, S. M. Girvin, and R. J. Schoelkopf, Observation of quantum state collapse and revival due to the single-photon Kerr effect, Nature (London) **495**, 205 (2013).

[87] A. P. Peirce, M. A. Dahleh, and H. Rabitz, Optimal control of quantum-mechanical systems: Existence, numerical approximation, and applications, Phys. Rev. A **37**, 4950 (1988).

[88] C. Brif, R. Chakrabarti, and H. Rabitz, Control of quantum phenomena: Past, present and future, New J. Phys. **12**, 075008 (2010).